Raman effects in quantum frequency conversion using Bragg scattering

Mathias L. H. Korsgaard ⓘ, Jacob G. Koefoed, and Karsten Rottwitt ⓘ*

Department of Electrical and Photonics Engineering, Technical University of Denmark, 2800 Kongens Lyngby, Denmark

We present a quantum-mechanical model that describes fiber-based frequency conversion by four-wave-mixing Bragg scattering in the presence of Raman interactions. In the case of continuous-wave pumps, we find closed-form expressions for the conversion efficiency and photon statistics characterized by the second-order correlation function. For pulsed pumps, we derive a highly general model based on Green functions and provide a numerical solution method using a split-step scheme. In both cases, we find that noise from spontaneous Raman scattering can pose a serious challenge to this type of frequency conversion if the pumps are less than 30 THz from the quantum fields. However, this impact can be mitigated with cross-polarized pumps and, on the anti-Stokes side, through fiber cooling.

I. INTRODUCTION

Quantum frequency conversion is a crucial component for future photon-based quantum communication and computing applications [1–4]. The ability to flexibly convert photons between wavelengths without destroying the fragile quantum states [5,6] provides an interface between different parts of a quantum-optical system such as a photon source, a transmission fiber, or a quantum memory [7].

Four-wave-mixing Bragg scattering (FWM-BS) provides a platform free of additional noise [8], ideal for quantum frequency conversion. Compared to the well-known processes of sum-frequency and difference-frequency generation [9,10], the two pump fields in FWM-BS provide increased flexibility [11]. In addition, FWM-BS is possible in optical fibers with efficient integration into an existing network [12,13]. This has proved to be a promising platform for frequency multiplexing of single photons [14] and has furthermore been used to demonstrate quantum interference between spectral channels [15,16].

Unfortunately, fiber-based FWM-BS is often accompanied by a broadband emission from spontaneous Raman scattering (SpRS) induced by nonlinear interactions of light and localized material vibrations [13,17]. This can be partly mitigated through cooling [12] and partly through restriction to short frequency shifts [13]. However, long frequency shifts require a strong pump that is spectrally close to the fragile quantum fields and thus necessitates a more careful analysis of the impact of Raman scattering. Appropriate quantum models exist in the context of photon-pair generation [18,19], but FWM-BS has only been studied using classical models [20] or with a full Lindblad approach [21] with the associated computational challenges.

In this work, we provide a semiclassical quantum model of FWM-BS in the presence of Raman scattering by exploiting the bilinear nature of the equations of motion. This leads to exact solutions for the quantum fields in terms of Green functions without needing to restrict the Hilbert space. Using this model, we provide quantitative guidelines for how the quality of frequency conversion depends on the system configuration. We study the photon statistics and spectral properties of converted single photons in the presence of Raman scattering for both continuous-wave (cw) pumping and pulsed pumping using a numerical split-step scheme.

II. THEORY

In this section, we introduce the evolution equations for the quantum and classical pumps and derive a general expression for the second-order correlation function for the frequency-converted light.

A. Frequency conversion using Bragg scattering

FWM-BS is the coherent interaction between four spectrally separated fields, as illustrated in Fig. 1(a). An input signal field (s) is frequency translated into the idler field (i) through a $\chi^{(3)}$-nonlinear interaction mediated by two strong pumps (p and q), under the requirement of energy conservation $\omega_i - \omega_s + \omega_p - \omega_q = 0$. For the remainder of our analysis, we assume that the separation $\Omega = \omega_i - \omega_s$ is within the Raman bandwidth, while the two pumps are separated sufficiently far that we may neglect Raman interactions over this frequency span (that is, there are no phonon modes with a sufficiently large frequency to mediate such interactions). For linearly polarized fields, the $\chi^{(3)}$-tensor distinguishes between two different polarization configurations of the fields: co-polarized and cross polarized, as illustrated in Fig. 1(a). The co-polarized configuration has the largest nonlinear strength and is therefore usually preferable [22]. However, the Raman response divides the cross-polarized configuration into two: the isotropic and anisotropic configurations [22]. These correspond to the fields within the Raman bandwidth of each other being co-polarized and cross polarized, respectively. The co-polarized configuration maximizes Raman scattering through the parallel Raman response, whereas the anisotropic minimizes it through the orthogonal Raman response. The
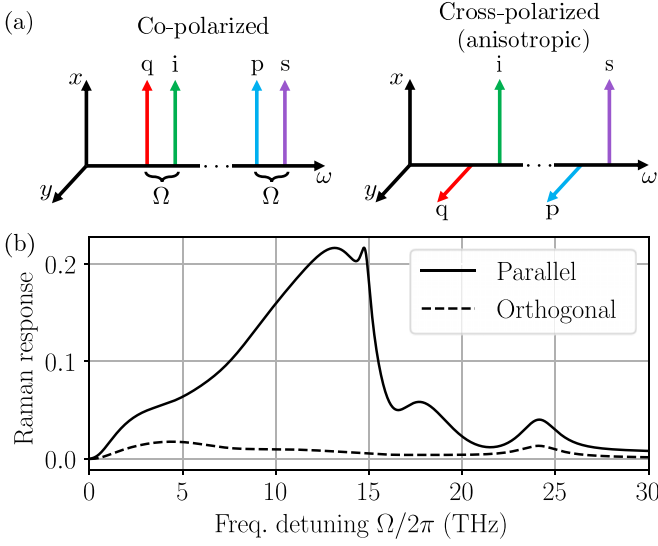
---

*Contact author: karo@dtu.dk

FIG. 1. (a) Illustration of two possible polarization configurations of the four fields: idler (i), signal (s), and pumps (p and q). The pumps are separated from the nearest quantum fields by a frequency detuning Ω. (b) The Raman response corresponding to the two polarization configurations for a silica fiber. The data are acquired from Refs. [22,24].

corresponding response functions for a silica fiber are illustrated in Fig. 1(b). For these reasons, we focus on the co-polarized and anisotropic configurations in the following analysis. It should be noted that these polarization configurations only hold for linearly polarized fields. The model presented in this paper is completely general and is therefore applicable for more complicated polarization modes, such as orbital angular momentum modes [23] and spatial mode configurations, although we only consider co-propagating modes. For the sake of simplicity, we focus on the linearly polarized modes during the presentation of the model.

B. Field equations

The full-vectorial quantum field equation describing FWM for quantum operators representing the two polarization components has been derived in previous papers [18,25]. In Appendix A, we have deduced the nonlinear coefficients and response functions when the quantum operators represent arbitrary spatial and polarization modes and find that the resulting equation of motion is identical to the full-vectorial quantum field equation. To model FWM-BS, we consider the four fields described in the previous section and only keep the FWM terms for which $\omega_p - \omega_q + \omega_i - \omega_s = 0$ is fulfilled. To simplify the equations, we decouple the pump equations from the signal and idler equations by letting the pumps be classical fields that are normalized such that $|A_{p,q}|^2$ is the power. This corresponds to an undepleted pump approximation. The quantum fields are normalized to have the standard equal-space commutation relations $[\hat{a}_n(z,t), \hat{a}_m^\dagger(z,t')] = \delta_{nm}\delta(t-t')$. The idler equation is thereby

$$\partial_z \hat{a}_i = -\beta_{1i}\partial_t \hat{a}_i - \frac{i}{2}\beta_{2i}\partial_t^2 \hat{a}_i$$
$$+ 2i(\gamma_{ip}|A_p|^2 + \gamma_{iq}|A_q|^2)\hat{a}_i + 2\gamma_{ipqs}A_p^*A_q\hat{a}_s$$

$$+ iA_q \int dt' f_{iqps}(t-t')A_p^*(z,t')\hat{a}_s(z,t')$$

$$+ iA_q \int dt' f_{iqqi}(t-t')A_q^*(z,t')\hat{a}_i(z,t') + i\hat{m}_{iq}A_q. \quad (1)$$

The indices are contracted such that ip = iiqq and the fields without an argument are evaluated in (z,t). The instantaneous electronic response is described by γ_{ijkl}, and the noninstantaneous Raman response is represented by f_{ijkl}, and each characterizes the interaction between the four fields i, j, k, and l. The noise operator $\hat{m}_{ij}$ describes the creation or annihilation of a phonon under the interaction between the two fields i and j and thereby represents SpRS. Both the Raman response function f_{ijkl} and the noise operator $\hat{m}_{ij}$ oscillate at frequency Ω, as described in Appendix A. In addition, the linear dispersion is expanded around the central idler frequency in terms of dispersion parameters β_{1i} and β_{2i}. In this model, we kept the terms responsible for linear dispersion up to second order, nonlinear phase modulation (NPM) from the pumps, FWM-BS, delayed FWM-BS, delayed NPM, and SpRS. We neglected the Raman terms that require interaction with a phonon at the large frequency separation, for example, SpRS from pump p to the idler. The signal field equation is identical under the substitution s ↔ i and p ↔ q. We note that unlike their electronic counterparts, the delayed versions of NPM and FWM-BS do not perfectly conserve the energy of the optical fields, leading to stimulated Raman effects.

The noise operators are based on the initial thermal phonon distribution and are thus completely determined by their second-order correlation,

$$\langle \hat{m}_{ij}^\dagger(z,\omega)\hat{m}_{kl}(z',\omega')\rangle = \delta(\omega-\omega')\delta(z-z')F_{ijkl}(\omega), \quad (2a)$$

$$F_{ijkl}(\omega) = \sqrt{2\pi}\,\mathrm{Im}[f_{ijkl}(\omega)]n_{\mathrm{th}}(\omega+\Omega), \quad (2b)$$

where $n_{\mathrm{th}}(\omega) = [\exp(\frac{\hbar\omega}{k_B T}) - 1]^{-1}$ is the thermal population number. Since the field equations are bilinear in the quantum fields, the solution takes the simple input-output form [26,27] after an interaction of length $z = \ell$,

$$\hat{a}_i(\ell,t) = \int dt' [G_{ii}(\ell,t,t')\hat{a}_i(0,t') + G_{is}(\ell,t,t')\hat{a}_s(0,t')]$$

$$+ i \int dt' \int_0^\ell dz' [A_q(z',t')G_{ii}(\ell-z',t,t')\hat{m}_{iq}(z',t')$$

$$+ A_p(z',t')G_{is}(\ell-z',t,t')\hat{m}_{sp}(z',t')], \quad (3)$$

where G_{ij} are Green functions. The first term here represents the frequency-conversion process, while the second term represents contamination from SpRS that is also subjected to the frequency-conversion effect after its creation.

The strong classical pumps are unaffected by the single-photon-level FWM-BS and are thus governed by

$$\partial_z A_p = -\beta_{1p}\partial_t A_p - \frac{i}{2}\beta_{2p}\partial_t^2 A_p$$

$$+ \gamma_p |A_p|^2 A_p + 2\gamma_{pq}|A_q|^2 A_p$$

$$+ iA_p \int dt' f_p(t-t')|A_p(z,t')|^2$$

$$+ iA_q \int dt' f_{pq}(t-t')|A_q(z,t')|^2. \quad (4)$$

The equation for pump q is found by substituting p ↔ q. By treating the pumps classically, the problem simplifies considerably since the equations of motions are now bilinear in the signal and idler fields. However, as a consequence of the delayed nonlinear response and the phonon operator, the optical-field commutators are no longer perfectly preserved. In Appendix B, we demonstrate the validity of the quantum model by showing that the commutators are preserved to first order in the Raman response. In this sense, the model is perturbative, which is the experimentally desired situation. This is most problematic on the Stokes side where the field operators are (classically) amplified instead of populating higher Fock states, and the spontaneous Raman scattering cannot be minimized in regard to the temperature. On the anti-Stokes side, which is the most experimentally relevant, this behavior is less problematic since the induced decay of the field operator simply lowers their expectation values with respect to the vacuum, while a lower temperature decreases the amount of spontaneous Raman scattering. Calculating the photon flux, the amplification and depletion are correctly captured; however, the second-order correlation function measures the photon statistics, which can therefore not be described properly under a classical amplification. Since the second-order correlation function is insensitive to loss, the photon statistics of classical depletion are accurately described.

C. Second-order correlation function

For single-photon applications, the second-order correlation function is an important metric. At the waveguide output $z = \ell$ and at times t_1, t_2, it is defined as

$$g^{(2)}(t_1, t_2) = \frac{\langle \hat{a}_i^\dagger(\ell, t_1) \hat{a}_i^\dagger(\ell, t_2) \hat{a}_i(\ell, t_2) \hat{a}_i(\ell, t_1) \rangle}{\langle \hat{a}_i^\dagger(\ell, t_1) \hat{a}_i(\ell, t_1) \rangle \langle \hat{a}_i^\dagger(\ell, t_2) \hat{a}_i(\ell, t_2) \rangle}. \quad (5)$$

At zero delay, a $g^{(2)}(t, t)$ value of close to 0 indicates strong antibunching and thus single-photon statistics at the output at time t. For a frequency-converted single photon, a value larger than 0 indicates contamination by Raman noise photons. We consider a single-photon input state with a temporal amplitude $\psi(t)$,

$$|\psi\rangle = \int dt \, \psi(t) \hat{a}_s^\dagger(t) |0\rangle, \quad (6)$$

for which the second-order correlation function is calculated (see Appendix C for details),

$$g^{(2)}(t_1, t_2) = \frac{1}{I_{out}(t_1) I_{out}(t_2)} \{ |\psi_{out}(t_1)|^2 E(t_2, t_2)$$
$$+ |\psi_{out}(t_2)|^2 E(t_1, t_1) + E(t_1, t_1) E(t_2, t_2)$$
$$+ 2\mathrm{Re}[\psi_{out}^*(t_1) \psi_{out}(t_2) E(t_1, t_2)] + |E(t_1, t_2)|^2 \}, \quad (7)$$

where the expectation values are determined in terms of the Green functions,

$$I_{out}(t) = |\psi_{out}(t)|^2 + E(t, t), \quad (8a)$$

$$\psi_{out}(t) = \int dt' G_{is}(\ell, t, t') \psi(t'), \quad (8b)$$

$$E(t_1, t_2) = \int_0^\ell dz \iint dt \, dt' Q^*(z, t_1, t) Q(z, t_2, t') F(t - t'), \quad (8c)$$

$$Q(z, t, t') = A_q(z, t) G_{ii}(z, t, t') + A_p(z, t) G_{is}(z, t, t'). \quad (8d)$$

We have assumed a balanced Raman response, $F = F_{iqqi} = F_{iqps}$, such that the Green functions can be factorized. Here, $F(t)$ is the inverse Fourier transform of $F(\omega)$. Thus, the problem of calculating $g^{(2)}$ is reduced to the calculation of the Green functions.

In realistic experiments, we cannot access $g^{(2)}(t_1, t_2)$ directly due to the finite temporal resolution of single-photon detectors. Instead, we measure photon detection events ("clicks") within a certain time window T. Thus, the experimentally relevant metric is instead [28]

$$g^{(2)}_{click} = \frac{\iint_{-T/2}^{T/2} dt_1 dt_2 \langle \hat{a}_i^\dagger(\ell, t_1) \hat{a}_i^\dagger(\ell, t_2) \hat{a}_i(\ell, t_2) \hat{a}_i(\ell, t_1) \rangle}{\left[\int_{-T/2}^{T/2} dt \langle \hat{a}_i^\dagger(\ell, t) \hat{a}_i(\ell, t) \rangle \right]^2}. \quad (9)$$

In the following sections, we analyze the second-order photon statistics of frequency-converted single photons in the presence of stimulated and spontaneous Raman scattering for both the case of cw pumps and the experimentally relevant case of pulsed pumps.

III. CONTINUOUS-WAVE PUMPS

In this section, we analyze the case of cw pumps where analytical solutions are obtained.

A. Signal and idler evolution

The cw pumps propagate with the pure phase evolution $A_{p,q}(z, t) = \sqrt{P_0} e^{i\phi(z)}$. Defining the Fourier transform as $\hat{a}_i(z, \omega) = \frac{1}{\sqrt{2\pi}} \int_{-\infty}^{\infty} dt \, \hat{a}_i(z, t) e^{i\omega t}$, we obtain the simple quantum evolution equation for the idler,

$$\partial_z \hat{a}_i(z, \omega) = i\kappa_i(z, \omega) \hat{a}_i(z, \omega)$$
$$+ ig(\omega) \hat{a}_s(z, \omega) + i\sqrt{P_0} \hat{m}_{iq}(z, \omega), \quad (10)$$

where the coupling functions are given by

$$\kappa_i(\omega) = \beta_i(\omega) + \sqrt{2\pi} P_0 f_{iqqi}(\omega) + \frac{\Delta\beta}{2}, \quad (11a)$$

$$g(\omega) = 2P_0 \gamma_{iqps} + \sqrt{2\pi} P_0 f_{iqps}(\omega). \quad (11b)$$

Here, the real part of κ_i describes phase modulation, while the imaginary part describes classical. amplification or depletion. The real part of $g(\omega)$ describes the gain in the idler field due to the frequency conversion and stimulated Raman scattering given by the imaginary part. The signal equation is found under the substitution i ↔ s, q ↔ p, and $\Delta\beta \to -\Delta\beta$. Due to the pumps being cw, the Green functions take the form $G_{ij}(\ell, t, t') = G_{ij}(\ell, t - t')$, and the solution in the frequency domain is thereby found,

$$\hat{a}_i(\ell, \omega) = G_{ii}(\ell, \omega) \hat{a}_i(0, \omega) + G_{is}(\ell, \omega) \hat{a}_s(0, \omega)$$
$$+ i\sqrt{P_0} \int_0^\ell dz [G_{ii}(\ell - z, \omega) \hat{m}_{iq}(z, \omega)$$
$$+ G_{is}(\ell - z, \omega) \hat{m}_{sp}(z, \omega)], \quad (12)$$

where the Green functions are given by

$$G_{\text{ii}}(z, \omega) = \frac{e^{\frac{i}{2}[\kappa_s(\omega) + \kappa_i(\omega)]z}}{k(\omega)} \left\{ k(\omega) \cos[k(\omega)z] \right.$$
$$\left. - \frac{i}{2} \Delta\beta(\omega) \sin[k(\omega)z] \right\}, \tag{13a}$$

$$G_{\text{is}}(z, \omega) = i \frac{g(\omega)}{k(\omega)} e^{\frac{i}{2}[\kappa_s(\omega) + \kappa_i(\omega)]z} \sin[k(\omega)z], \tag{13b}$$

and we have defined the effective coupling function due to phase mismatch, field walk-off, and higher-order dispersion as

$$k(\omega) = \frac{1}{2}\sqrt{4g(\omega)^2 + \Delta\beta(\omega)^2}. \tag{14}$$

From the explicit expressions of the Green functions, the classical amplification or depletion of the quantum fields is seen to enter through the imaginary part of $\kappa_{s,i}$ and k.

1. Spectral filtering

In practice, the idler is filtered spectrally to reduce the amount of spontaneously emitted Raman photons. The filtered quantum field after the nonlinear interaction is written as

$$\hat{a}_{\text{i}}(\ell, t) = \frac{1}{\sqrt{2\pi}} \int_{-\infty}^{\infty} d\omega H(\omega) \hat{a}_{\text{i}}(\ell, \omega) e^{-i\omega t}, \tag{15}$$

where $H(\omega)$ is the spectral filter transmission function, which is centered around the center frequency of the idler. The output temporal distribution of the photon state is thereby

$$\psi_{\text{out}}(t) = \frac{1}{2\pi} \int dt' \int d\omega H(\omega) G_{\text{is}}(\ell, \omega) \psi(t') e^{-i\omega(t-t')}. \tag{16}$$

The expectation value of the phonon operators is similarly found to be

$$E(t_1, t_2) = \frac{P_0}{\sqrt{2\pi}} \int_0^\ell dz \int d\omega |H(\omega)|^2$$
$$\times |G_{\text{ii}}(z, \omega) + G_{\text{is}}(z, \omega)|^2 F(\omega) e^{-i\omega(t_1-t_2)}. \tag{17}$$

In the following, we consider a rectangular spectral filter with spectral width $\Delta\omega$.

2. Linearly polarized fields

The results presented in the previous sections are completely general as they describe any field mode or polarization. In the following examples of the model, we restrict our attention to the experimentally relevant situation of linearly polarized fields. Additionally, we parametrize the response functions through the Raman fraction f_R, which describes the fraction of the nonlinear response that is attributed to Raman scattering. For silica fibers, which will be our focus of interest, $f_R \approx 0.18$ [29]. The electronic and Raman response functions thereby take the form [18]

$$\gamma_{ijkl} = \frac{1}{2}\gamma(1 - f_R)(\delta_{ij}\delta_{kl} + \delta_{ik}\delta_{jl} + \delta_{il}\delta_{jk}), \tag{18a}$$

$$f_{ijkl}(t) = \gamma f_R e^{i\Omega t} [h_a(t)\delta_{ij}\delta_{kl} + \frac{1}{2}h_b(t)(\delta_{ik}\delta_{jl} + \delta_{il}\delta_{jk})], \tag{18b}$$
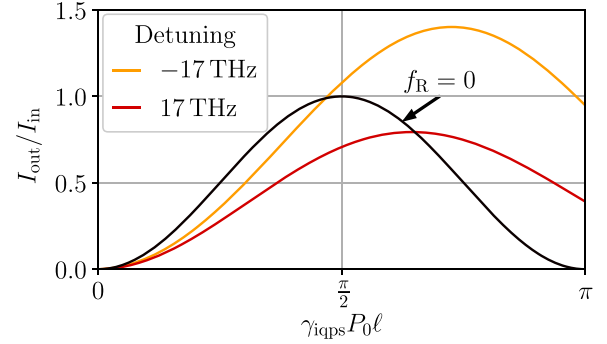

FIG. 2. The relative output flux, as a function of the dimensionless nonlinear interaction strength $\gamma P_0 \ell$ in a co-polarized configuration. The colored lines include Raman scattering and are illustrated for $f_R = 0.18$, detuning $\Omega/2\pi$, and $\Delta\omega/I_{\text{in}} = 1$.

where the indices on the Kronecker deltas refer to the polarization of the corresponding mode, and γ depends on the spatial mode overlap of the field profiles, as described in Appendix A. In the remaining, we assume a single-mode fiber such that γ is the same for NPM and Bragg scattering. Throughout, we use the nonlinear coefficient of silica, $\gamma \approx 1 \, (\text{W km})^{-1}$ [30]. The sum of the isotropic-orthogonal h_a and anisotropic-orthogonal h_b Raman response gives the parallel response h, which can be estimated as a sum of harmonic oscillators,

$$h(t) = \Theta(t) \sum_i F_i d_i \sin(\omega_i t) e^{-d_i t}, \tag{19}$$

where $\Theta(t)$ is the Heaviside step function, ω_i is the resonance frequency of the phonons, F_i is the resonance amplitude, and d_i is the phonon decay rate. Using 11 oscillators provides a good approximation for the silica Raman response function [24]. From the parallel response function, we extract the anisotropic response function using Ref. [22].

B. Photon flux

To illustrate how Raman scattering impacts the general frequency-conversion process, we start by investigating the frequency-converted photon flux I_{out}. We consider a single photon with a spectral width much smaller than the variations of the Raman response, being $\frac{1}{\tau_p} \ll \min\{d_i\}$. The filter width is correspondingly decreased, such that $\Delta\omega \ll \min\{d_i\}$. For the remainder of this section, we assume perfect phase matching $\Delta\beta(\omega) = 0$ corresponding to $k(\omega) = g(\omega)$. To first order in the filter width, the output flux thereby becomes

$$I_{\text{out}} = |G_{\text{is}}(\ell, \omega = 0)|^2 I_{\text{in}}$$
$$+ \frac{\Delta\omega}{4\sqrt{2\pi}} \{1 - \exp[-8\pi f_R R(0)\gamma P_0 \ell]\} n_{\text{th}}(\Omega), \tag{20}$$

where $\text{Im}\{f(\omega)\} = \sqrt{2\pi}\gamma f_R R(\omega)$, and the indices have been suppressed for compactness. In Fig. 2, the relative output flux is shown as a function of the dimensionless nonlinear interaction strength $\gamma_{\text{iqps}}P_0 \ell$, in a Stokes ($\Omega/2\pi = -17$ THz) and an anti-Stokes ($\Omega/2\pi = 17$ THz) configuration, with $f_R = 0.18$. These are compared to the relative output flux in the absence of Raman scattering, $f_R = 0$.

The optimal interaction strength in the absence of Raman scattering is given by $\gamma_{\mathrm{iqps}} P_0 \ell = \frac{\pi}{2}$, as can be seen directly from the Green function G_{is}. As Raman scattering is introduced, the relative output flux significantly depends on the frequency detuning. Due to stimulated Raman scattering, the Stokes configuration experiences gain, whereas the anti-Stokes configuration experiences depletion. The impact of stimulated Raman scattering can be seen more easily through the explicit expression of the Green function,

$$|G_{\mathrm{is}}|^2 = \frac{e^{-2\mathrm{Im}\{\kappa\}\ell}}{2} \{\cosh[2\mathrm{Im}(g)\ell] - \cos[2\mathrm{Re}(g)\ell]\}. \quad (21)$$

The imaginary part of the cross-field coupling function g induces a gain through Raman-induced Bragg scattering, effectively constituting a four-field stimulated Raman scattering effect. However, the imaginary part of the self-field coupling function κ introduces gain or absorption, depending on the sign of Ω, and is the well-known stimulated Raman scattering effect. Evidently, stimulated absorption requires an anti-Stokes configuration, corresponding to $\mathrm{Im}\{\kappa\} > 0$ and $\mathrm{Im}\{g - \kappa\} < 0$. In the examples presented here, we consider a balanced Raman response, $\mathrm{Im}\{g - \kappa\} = 0$. To see the impact of spontaneous Raman scattering, it is necessary to investigate the second-order correlation function.

C. Second-order correlation

Having determined the output probability amplitude ψ_{out} and the phonon expectation value, given by Eq. (17), the second-order correlation function is directly determined by Eq. (7). We choose to investigate an input state with a Gaussian temporal amplitude, given by

$$\psi(t) = \frac{1}{\sqrt{\tau_p}(2\pi)^{\frac{1}{4}}} e^{-\frac{t^2}{4\tau_p^2}}, \quad (22)$$

where τ_p is the standard deviation of the probability distribution $|\psi|^2$. For the present analysis, we focus on photon pulses with a duration of the order of the Raman response, $\tau_p = 0.1$ ps. The filter width is chosen corresponding to the pulse duration $\Delta\omega = \frac{2}{\tau_p}$, so that the photon with high probability passes through the filter.

In Fig. 3(a), the second-order correlation function given by Eq. (7) is shown. Along the dashed line in Fig. 3(b), the $g^{(2)}$ value at zero delay time $g^{(2)}(t, t)$ is found. From this, the idler field is seen to exhibit single-photon statistics when the single photon is present, $|t_1| = |t_2| < \tau_p$. Outside the time window of the single photon, the idler field exhibits thermal statistics, which indicates the presence of spontaneous Raman photons, which are inherently thermal. The solid line in Fig. 3(b) corresponds to the $g^{(2)}$ value as a function of delay time, measured exactly at the single-photon peak.

We now consider the experimentally relevant time-resolved $g_{\mathrm{click}}^{(2)}$ value with a time window of 10 ps, of the order of realistic detector resolutions [31]. In Fig. 4(a), $g_{\mathrm{click}}^{(2)}$ is shown as a function of the nonlinear interaction strength with a varying interaction length, for a frequency detuning of $\Omega/2\pi = 17$ THz and a fiber temperature of 300 K. Initially, the field is dominated by spontaneous Raman photons, which is characterized by a value of $g_{\mathrm{click}}^{(2)} \sim 1$. Here, the thermal statistics are
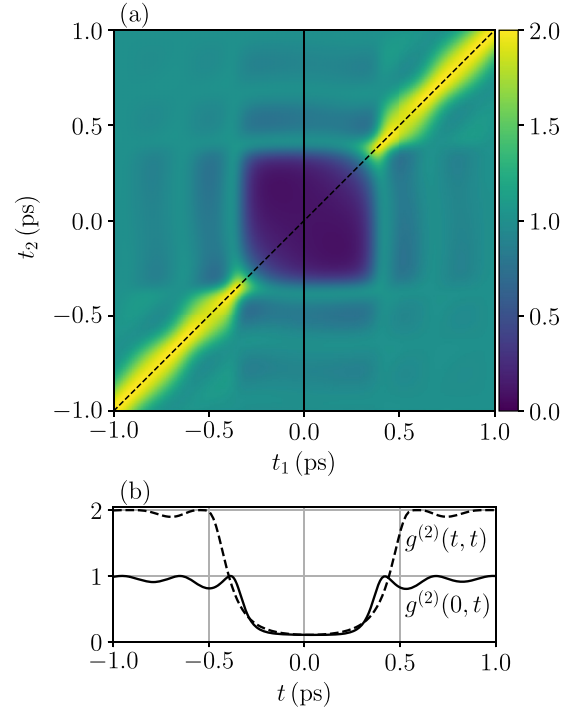

FIG. 3. (a) The second-order correlation function $g^{(2)}(t_1, t_2)$ illustrated for $\tau_p = 0.1$ ps, $f_{\mathrm{R}} = 0.18$, $\Omega/2\pi = 17$ THz, and a temperature of 300 K. (b) The cross sections of $g^{(2)}$ given by the solid and dashed lines in (a).

not apparent since the thermal correlations are much shorter than the detector window due to the broadband nature of the Raman spectrum. As the interaction length increases, $g_{\mathrm{click}}^{(2)}$ decreases, indicating the conversion of the single photon. The anisotropic polarization configuration yields a significantly lower $g_{\mathrm{click}}^{(2)}$ value, compared to the co-polarized configuration, even though the appropriate interaction length is a factor of three larger. This is primarily caused by the orthogonal Raman response being approximately a factor of 10 smaller. The optimal $g_{\mathrm{click}}^{(2)}$ value is not obtained at the optimal interaction length due to the linear increase in spontaneously generated Raman photons.

In Fig. 4(b), $g_{\mathrm{click}}^{(2)}$ is shown as a function of frequency detuning at the optimal interaction length, for three different temperatures and the two polarization configurations. The Raman response is clearly present for the two larger temperatures, which again shows the significance of the anisotropic response. At 22 THz, the $g_{\mathrm{click}}^{(2)}$ value is comparable for the two polarization configurations due to a small difference in the Raman responses [see Fig. 1(b)], while the interaction length for the anisotropic configuration is still a factor of 3 larger. For the low temperature 4 K, the phonon occupation is almost nonexistent, thereby suppressing the amount of spontaneous Raman scattering.

In the example presented here, the single-photon duration is of the order of the Raman response, ~ 0.1 ps. However, single photons produced by quantum dots are usually of the order of nanoseconds, permitting a filter width of the order of GHz [32]. We therefore consider the regime in which the spectral filter width $\Delta\omega$ is much smaller than the
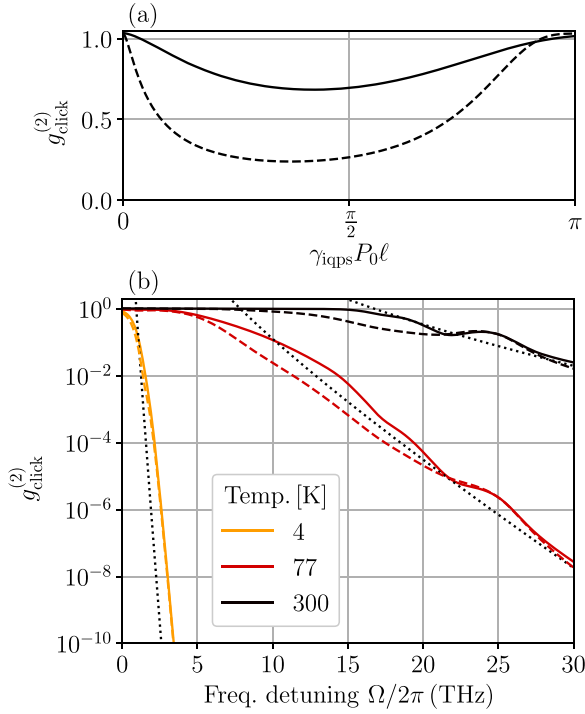
FIG. 4. (a) The time-resolved second-order correlation value $g^{(2)}_{\text{click}}$ as a function of nonlinear interaction strength, with $\gamma P_0 = 1\,(\text{km})^{-1}$, $f_{\text{R}} = 0.18$, a fiber temperature of 300 K, and a frequency detuning of $\Omega/2\pi = 17$ THz. (b) $g^{(2)}_{\text{click}}$ as a function of frequency detuning. This is illustrated for the co-polarized (solid line) and the anisotropic (dashed line) polarization configuration, for three different fiber temperatures. The black dotted lines correspond to the approximated $g^{(2)}_{\text{click}}$ value, given by Eq. (23), for the corresponding temperatures.

variations of the Raman response. Additionally, we assume that the photon is completely captured both spectrally and temporally, such that $T\Delta\omega \gg 1$. Finally, we assume that the effect of the spontaneous Raman photons is smaller than the frequency conversion of the single photon corresponding to $|T\Delta\omega f_{\text{R}}\ell\gamma P_0\ell R(0)| \ll 1$. Under these three assumptions, we obtain the approximate result,

$$g^{(2)}_{\text{click}} \approx (T\Delta\omega + 2\pi)\sqrt{2\pi}R(0)n_{\text{th}}(\Omega)f_{\text{R}}\gamma P_0\ell. \quad (23)$$

Evidently, $g^{(2)}_{\text{click}}$ is proportional to $R\,n_{\text{th}}$, which is the spontaneous Raman spectrum. In the regime $|\Omega| \to \infty$, the Raman response can be expanded in a Laurent series such that $R(0) \approx \frac{1}{\Omega^3}\sum_i F_i\omega_i d_i^2$, which is used in Fig. 4(b) to illustrate the approximated $g^{(2)}_{\text{click}}$ value, given by Eq. (23), as the black dotted lines. Even though $\Delta\omega/2\pi = 20$ THz is much larger than the variations of the Raman response in Fig. 4(b), the approximated $g^{(2)}_{\text{click}}$ value estimates the order of magnitude for the exact value, for the temperatures 300 K and 77 K. However, for 4 K, the approximation error is emphasized due to n_{th} being small.

The analytical results show that it is possible to achieve a second-order correlation value on the single-photon level within the Raman bandwidth by properly engineering the fields through frequency detuning, polarization configuration, and fiber temperature. However, using pulsed pumps unlocks

additional degrees of freedom, and we consider this case in the following section.

IV. PULSED PUMPS

In this section, we present a general evolution equation for the Green functions introduced in Eq. (3). In contrast to previous approaches, which involve propagating modes of a Schmidt decomposition without Raman scattering [33,34], we directly solve for the Greens function. We obtain the governing equations by inserting the proposed solution given by Eq. (3) into Eq. (1). The resulting Green function equation is expressed as a vector equation of the form

$$\left(\partial_z + \underline{\beta}_1\partial_t + \frac{i}{2}\underline{\beta}_2\partial_t^2\right)\mathbf{G}(z,t,t') = i\int d\tau\underline{\mathbf{K}}(z,t,\tau)\mathbf{G}(z,\tau,t'),$$
$$(24)$$

where the Green function vector and dispersion coefficient matrices are given by

$$\mathbf{G}(z,t,t') = \begin{pmatrix} G_{\text{ii}}(z,t,t') \\ G_{\text{si}}(z,t,t') \end{pmatrix}, \qquad \underline{\beta}_n = \begin{pmatrix} \beta_{n\text{i}} & 0 \\ 0 & \beta_{n\text{s}} \end{pmatrix}. \quad (25)$$

The coupling matrix $\underline{\mathbf{K}}$ has an instantaneous and noninstantaneous part, representing the electronic $\underline{\mathbf{K}}_{\text{E}}$ and Raman $\underline{\mathbf{K}}_{\text{R}}$ response, respectively. These are given by

$$\underline{\mathbf{K}}(z,t,t') = \underline{\mathbf{K}}_{\text{E}}(z,t)\delta(t-t') + \underline{\mathbf{K}}_{\text{R}}(z,t,t'), \quad (26a)$$

$$\underline{\mathbf{K}}_{\text{E}}(z,t) = \begin{pmatrix} K^{\text{E}}_{\text{iqqi}}(z,t) & K^{\text{E}}_{\text{iqps}}(z,t)e^{i\Delta\beta z} \\ K^{\text{E}}_{\text{spqi}}(z,t)e^{-i\Delta\beta z} & K^{\text{E}}_{\text{spps}}(z,t) \end{pmatrix}, \quad (26b)$$

$$\underline{\mathbf{K}}_{\text{R}}(z,t,t') = \begin{pmatrix} K^{\text{R}}_{\text{iqqi}}(z,t,t') & K^{\text{R}}_{\text{iqps}}(z,t,t')e^{i\Delta\beta z} \\ K^{\text{R}}_{\text{spqi}}(z,t,t')e^{-i\Delta\beta z} & K^{\text{R}}_{\text{spps}}(z,t,t') \end{pmatrix},$$
$$(26c)$$

where the matrix elements are defined as

$$K^{\text{E}}_{ijkl}(z,t) = 2\gamma_{ijkl}A^*_k(z,t)A_j(z,t), \quad (27a)$$

$$K^{\text{R}}_{ijkl}(z,t,t') = f_{ijkl}(t-t')A^*_k(z,t')A_j(z,t). \quad (27b)$$

For the present analysis, the equations for G_{ii} and G_{si} are sufficient since $G_{\text{is}} = G^\dagger_{\text{si}}$. However, the equation for the two remaining Green functions is found under the substitution i $\leftrightarrow$ s and q $\leftrightarrow$ p. From Eq. (3), the initial condition to the Green function equation is inferred and is given by

$$\mathbf{G}(z=0,t,t') = \begin{pmatrix} 1 \\ 0 \end{pmatrix}\delta(t-t'). \quad (28)$$

The Green functions depend on the evolving pump fields. Therefore, to solve the Green function equation, it is necessary to simultaneously solve Eq. (4), which is carried out in the following using the conventional split-step Fourier method [35]. Before giving an example of the solutions, we outline how the split-step Fourier method is applied to the Green function equation.

A. Split-step scheme for Green functions

In this section, we describe a completely general split-step scheme for solving the Green function equation. The spatial
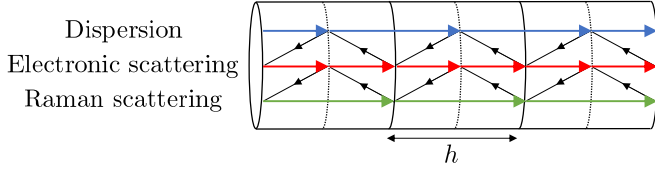
FIG. 5. Illustration of the incremental evolution of the three operators in the split-step scheme, applied on three iterated steps. Starting from the first $\frac{h}{2}$-dispersion step, the black arrows illustrate the chronological order of the scheme.

evolution of the Green functions can be expressed as

$$\partial_z \mathbf{G}_z = (D + E_z + R_z)\mathbf{G}_z, \qquad (29)$$

where D, E_z, and R_z are operators representing dispersive effects, and electronic and Raman-induced NPM and Bragg scattering at position z, respectively. The operators only act on the first time argument, as described by Eq. (24). Solving the equation over an increment h and invoking the trapezoidal rule to approximate the integral in the exponential, the formal solution can be expressed as

$$\mathbf{G}_{z+h} = \exp[Dh + \tilde{E}_z h + \tilde{R}_z h]\mathbf{G}_z + O(h^3), \qquad (30)$$

where $\tilde{O}_z = \frac{1}{2}(O_{z+h} + O_z)$. From here, the Baker-Hausdorf formula [35] can be applied twice, thereby separating the evolution of each of the physical effects, giving rise to a symmetrical split-step scheme with three operators and a local step error of $O(h^3)$. In Fig. 5, the symmetrical split-step scheme is illustrated for a single step and the consecutive application of the scheme. Each step is propagated by determining the impact of each operator, which is found by solving the equation for each physical effect. The dispersive and electronic effects have the exact solutions

$$[\mathrm{e}^{D_z h}\mathbf{G}_z](\omega, t') = \exp\left[i\left(\underline{\beta}_1 \omega + \frac{1}{2}\underline{\beta}_2 \omega^2\right)h\right]\mathbf{G}_z(\omega, t'), \quad (31a)$$

$$[\mathrm{e}^{\tilde{E}_z h}\mathbf{G}_z](t, t') = \begin{pmatrix} \mathcal{G}_{\mathrm{ii}}(z, t) & \mathcal{G}(z, t) \\ -\mathcal{G}^*(z, t) & \mathcal{G}_{\mathrm{si}}(z, t) \end{pmatrix}\mathbf{G}_z(t, t'), \quad (31b)$$

where the frequency argument in the dispersive step implies a Fourier transform. We have defined the matrix elements of the electronic step as

$$\mathcal{G}_{\mathrm{ii}}(z, t) = \frac{\mathrm{e}^{ik_1(z,t)h - \frac{i}{2}\Delta\beta h}}{k_2(z, t)}\left\{k_2(z, t)\cos[k_2(z, t)h]\right.$$
$$\left. + \frac{i}{2}\left[\tilde{K}^{\mathrm{e}}_{\mathrm{iqqi}}(z, t) - \tilde{K}^{\mathrm{e}}_{\mathrm{spps}}(z, t) + \Delta\beta\right]\sin[k_2(z, t)h]\right\},$$
$$(32a)$$

$$\mathcal{G}(z, t) = i\frac{\tilde{K}^{\mathrm{e}}_{\mathrm{iqps}}(z, t)}{k_2(z, t)}\mathrm{e}^{ik_1(z,t)h - \frac{i}{2}\Delta\beta h}\sin[k_2(z, t)h], \quad (32b)$$

$$k_1(z, t) = \frac{1}{2}\left[\tilde{K}^{\mathrm{e}}_{\mathrm{iqqi}}(z, t) + \tilde{K}^{\mathrm{e}}_{\mathrm{spps}}(z, t)\right], \qquad (32c)$$

$$k_2(z, t) = \frac{1}{2}\left\{4\left|\tilde{K}^{\mathrm{e}}_{\mathrm{iqps}}(z, t)\right|^2\right.$$
$$\left. + \left[\tilde{K}^{\mathrm{e}}_{\mathrm{iqqi}}(z, t) - \tilde{K}^{\mathrm{e}}_{\mathrm{spps}}(z, t) + \Delta\beta\right]^2\right\}^{1/2}, \qquad (32d)$$

where $\mathcal{G}_{\mathrm{si}}$ is found from $\mathcal{G}_{\mathrm{ii}}$ by substituting $\mathrm{i} \leftrightarrow \mathrm{s}$, and $\Delta\beta \to -\Delta\beta$. The tilde denotes the average over the z and $z + h$

points. Notably, the solution to the pure electronic scattering has the same form as the solution in the cw regime.

Finally, we solve the Raman step. The equation governing this step is an integro-differential equation, which has a form that does not have a general analytical solution. The equation can be solved using numerical ODE solvers; however, here we propose a simple iterative approach. We start by integrating $\hat{R}_z \mathbf{G}_z$ over the increment h, and invoking the trapezoidal rule to approximate the z integral,

$$[\mathrm{e}^{\tilde{R}_z h}\mathbf{G}_z](t, t') = \mathbf{G}_z(t, t') + \Delta\mathbf{G}_z(t, t'), \qquad (33a)$$

$$\Delta\mathbf{G}_z(t, t') = i\frac{h}{2}\int \mathrm{d}\tau[\underline{\mathbf{K}}_{\mathrm{R}}(z, t, \tau)\mathbf{G}_z(\tau, t')$$
$$+ \underline{\mathbf{K}}_{\mathrm{R}}(z + h, t, \tau)\mathbf{G}_{z+h}(\tau, t')]. \quad (33b)$$

We determine $\Delta\mathbf{G}_z$ recursively by first assuming $\mathbf{G}_{z+h} = \mathbf{G}_z$. After three iterations, the error is $O(h^3)$, which is consistent with the error of the symmetric split-step scheme.

B. Numerical results

In this section, we apply the scheme developed in the previous section to the simple case of an optical fiber with the fields placed symmetrically around the zero-dispersion line. The fields thus co-propagate pairwise with $\beta_{1\mathrm{s}} = \beta_{1\mathrm{q}}$ and $\beta_{1\mathrm{i}} = \beta_{1\mathrm{p}}$, and walk-off $\beta_{1\mathrm{s}} - \beta_{1\mathrm{i}} = \frac{\Delta n_{\mathrm{eff}}}{c}$, where c is the speed of light and we choose $\Delta n_{\mathrm{eff}} = 10^{-3}$. For simplicity, the input pumps are chosen to be identical to a Gaussian pulse form,

$$A_{\mathrm{q,p}}(0, t) = \sqrt{P}\exp\left[\frac{-\left(t \pm \frac{\Delta t}{2}\right)^2}{4\tau_{\mathrm{p}}^2}\right], \qquad (34)$$

where P is the peak power, τ_{p} is the pulse duration, and Δt is the initial separation between the pumps. The fiber length is chosen so that the pump fields collide at the fiber midpoint, corresponding to $\ell = \frac{2\Delta t c}{\Delta n_{\mathrm{eff}}}$, and to ensure complete pump-pump collision, we choose $\Delta t = 6\tau_{\mathrm{p}}$. To highlight the phonon-induced temporal dynamics, we only consider pulse durations of the order of the Raman response, $\tau_{\mathrm{p}} = 0.1$ ps.

In Fig. 6, the cross-Green function is illustrated for $\gamma P\ell = 4\pi$, which ensures full conversion for a suitably chosen input shape. Lines of causality, illustrated by the white dashed lines, inherently bound the cross-Green function for a pure electronic response due to the instantaneous nature of the electrons. The lines are given by $t_{\mathrm{i,s}} = t' + \beta_{1\mathrm{i,s}}\ell$, with t_{i} being the upper line and t_{s} the lower line, corresponding to the earliest and latest times at which a frequency-converted photon can arrive. Figure 6(a) shows $|G_{\mathrm{is}}|$ for a pure electronic response. It is characterized by the shape of the pump and a ripple. The same behavior has been observed in the analytical solutions, which have previously been determined for a pure electronic response, where the ripple enters through the zeroth-order Bessel function of the first kind [36]. Introducing second-order dispersion in Fig. 6(b), a complicated overlying pattern appears due to interference between the possible paths of conversion. In Figs. 6(c) and 6(d), Raman scattering is included with $f_{\mathrm{R}} = 0.18$ and $f_{\mathrm{R}} = 1$, respectively. For $f_{\mathrm{R}} = 0.18$, the Green function is mildly distorted, while for $f_{\mathrm{R}} = 1$, the Green function is significantly altered and extends beyond
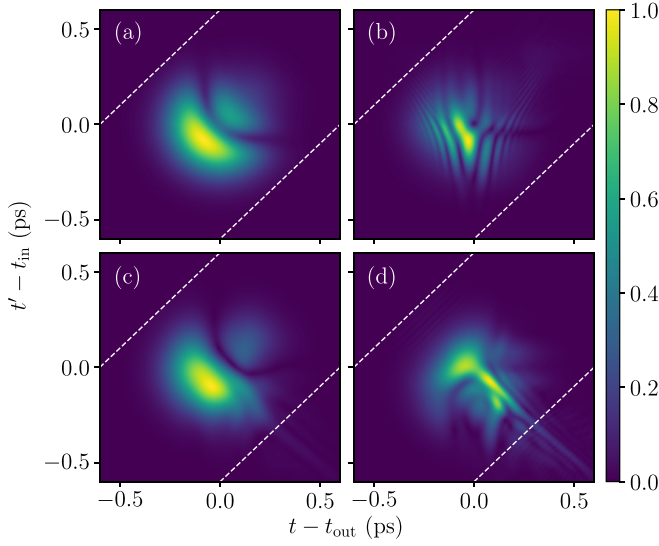
FIG. 6. The cross-Green functions $|G_{\mathrm{is}}|$ illustrated for four choices of parameters, each normalized to their respective maximum. (a) Pure electronic response $f_{\mathrm{R}} = 0$. (b) Pure electronic response $f_{\mathrm{R}} = 0$ and second-order dispersion $\beta_{2\mathrm{s,p}} = -\beta_{2\mathrm{i,q}} = 0.01 \frac{\mathrm{ps}^2}{\mathrm{m}}$. (c) Raman fraction corresponding to a silica fiber, $f_{\mathrm{R}} = 0.18$. (d) Pure Raman response $f_{\mathrm{R}} = 1$.
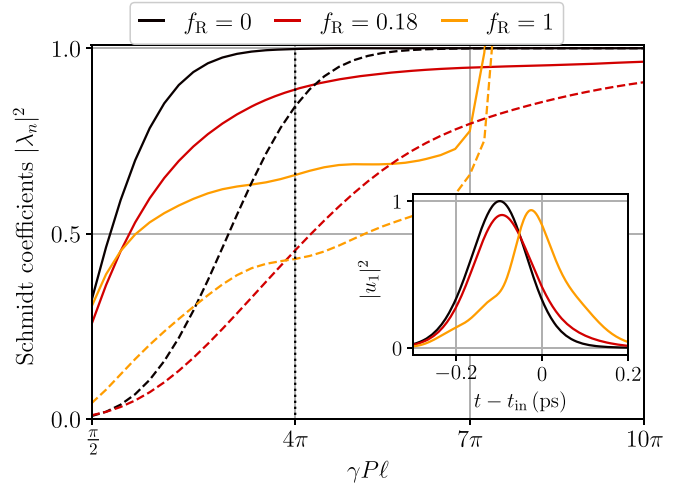

FIG. 7. The first (solid line) and second (dashed line) Schmidt mode coefficients as a function nonlinear interaction strength $\gamma P \ell$ found by varying the pump peak power P. These are shown for three choices of Raman fraction: pure electronic response $f_{\mathrm{R}} = 0$, silica fiber $f_{\mathrm{R}} = 0.18$, and pure Raman response $f_{\mathrm{R}} = 1$. Inset: The first-order input Schmidt mode for each of the three responses, evaluated at $\gamma P \ell = 4\pi$.

the slow (electronic) causality line due to a delay induced by the noninstantaneous Raman response.

To investigate the temporal dynamics, it is convenient to decompose the Green functions into Schmidt modes, which explicitly reveal the temporal shapes that are converted. The Schmidt decomposition of the Green function has the form [36,37],

$$G_{\mathrm{is}}(t, t') = \sum_n \lambda_n v_n(t) u_n(t'), \qquad (35)$$

where λ_n is the Schmidt coefficient describing the weight of each Schmidt mode, v_n is the output mode, and u_n is the input mode. If the nth input Schmidt mode is chosen as the input, it is converted to the corresponding nth output Schmidt mode with conversion efficiency $|\lambda_n|^2$. In Fig. 7, the Schmidt coefficients for the two first Schmidt modes are shown as a function of the nonlinear interaction strength $\gamma P \ell$, for three choices of f_{R}. For the pure electronic response $f_{\mathrm{R}} = 0$, the first-order Schmidt coefficient initially dominates, indicating a separable Green function in the low-interaction regime. As $\gamma P \ell$ increases, the second-order Schmidt coefficient becomes significant, which is seen as the emergence of a ripple in the Green function; see Fig. 6(a). For sufficiently large nonlinear interaction strength, both Schmidt modes are perfectly converted. The same behavior was observed in analytical models [36].

Introducing Raman scattering, $f_{\mathrm{R}} = 0.18$, the Schmidt coefficients decrease primarily due to absorption from stimulated Raman scattering. For $f_{\mathrm{R}} = 1$, the absorption is more significant and, notably, the second-order Schmidt coefficient increases faster initially, indicating that Raman scattering deteriorates the separability of the Green function. Around $\gamma P \ell = 7\pi$, the gains induced by phonon-mediated FWM and absorption from stimulated Raman scattering no longer

balance each other due to phase-modulation effects in the pumps, which give rise to an exponential increase of the Schmidt coefficients.

The inset in Fig. 7 shows the first-order input Schmidt modes for the three choices of f_{R}, evaluated for $\gamma P \ell = 4\pi$. The input Schmidt modes, including Raman scattering, acquire a slight temporal broadening due to the delayed Raman response, which thereby converts more efficiently before the point of collision compared to the pure electronic response.

Using the Green functions, we can directly determine the second-order correlation value $g_{\mathrm{click}}^{(2)}$ from Eq. (9). Figure 8 shows $g_{\mathrm{click}}^{(2)}$ for a fiber with $f_{\mathrm{R}} = 0.18$, temperature of 300 K, and a nonlinear interaction strength $\gamma P \ell = 4\pi$ for four choices of input pulses, as a function of the frequency detuning Ω. For comparison, we have included the case with cw pumps from the previous section. The output quantum states are filtered spectrally, as described by Eq. (15). The four choices of input pulses represent four methods for optimizing the single-photon shape with respect to the pumps.

The most primitive choice, which is the Gaussian, ensures the single photon has the same shape and duration as the pumps. This leads to poor performance due to the complicated phase-modulation effects of the pumps. We take the electronically induced phase modulation into account by choosing the input shape to be the first-order Schmidt mode of G_{is} with $f_{\mathrm{R}} = 0$, illustrated by the black line in the inset in Fig. 7. This noticeably improves the $g_{\mathrm{click}}^{(2)}$ value. Including the effects of Raman scattering, by choosing the input Schmidt mode with $f_{\mathrm{R}} = 0.18$, as illustrated by the red line in the inset in Fig. 7, improves the value even further. However, only by taking the filter into account in the Green function, is it possible to achieve the best performance.
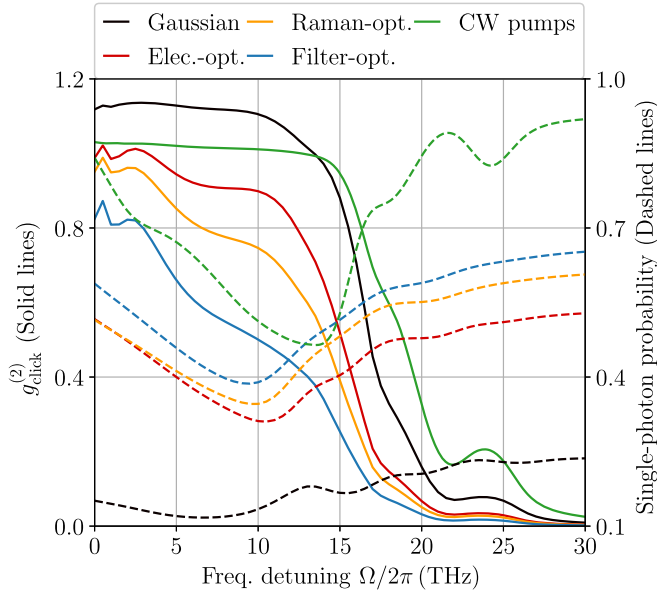
FIG. 8. Left axis: The time-resolved second-order correlation value $g_{\text{click}}^{(2)}$ for a fiber temperature of 300 K. Right axis: The probability of detecting a frequency-converted single-photon, as a function of frequency detuning. These are shown for four choices of input single-photon distributions being a Gaussian centered around t_{in}, an electronic optimized, a Raman optimized, and a filter optimized. The green curves illustrate the case with a Gaussian input pulse and cw pumps, from Fig. 4(b).

For all frequency detunings of interest, the cw case has the worst performance. This is because the average pump power over the detection window is larger for the cw pumps, which increases the accumulated spontaneous Raman photons.

This preliminary analysis shows that it is necessary to consider all physical effects to achieve the best possible frequency conversion. However, in a realistic experiment, the single-photon shape is often predetermined and the pump shapes would therefore have to be optimized with respect to this. Although this inverse problem is generally difficult to tackle, the present model paves the way for determining the optimal pump shapes by taking the relevant physical effects into account.

V. DISCUSSION AND CONCLUSION

In this paper, we have presented a general quantum-mechanical model that describes the frequency conversion of a quantum state in a medium constrained by Raman scattering. We have presented the model using a simple configuration with linearly polarized modes and a single-mode fiber. However, the generality of the model allows the modeling of frequency conversion between complicated spatial and polarization modes by using the appropriate coefficients, which can be found using the expressions provided in Appendix A.

Our focus of interest has been on the impact of Raman scattering on single-photon applications of Bragg scattering. Therefore, the appropriate figure of merit is the second-order correlation function, for which we determined an expression in terms of Green functions.

Using cw pumps, we found analytical expressions of the Green functions in the frequency domain, from which we have shown that it is possible to mitigate the impact of Raman scattering by cooling the fiber, adjusting the frequency detuning, or choosing a cross-polarized field configuration. The results show that it is not possible to achieve a reasonable $g_{\text{click}}^{(2)}$ value within the Raman bandwidth at room temperature. At the same time, previous studies have shown that a frequency beyond the Raman bandwidth is experimentally challenging due to increasing phase-matching sensitivity [38]. Using the approximate results for the cw model, given by Eq. (23), it is possible to acquire a preliminary estimate of the temperature required to achieve a $g_{\text{click}}^{(2)}$ value on the single-photon level, which we here consider as a value below 0.05: at the dominant Raman peak, $\Omega = 13$ THz, with a co-polarized configuration, a temperature of ~ 135 K is necessary, while a temperature of ~ 253 K is sufficient with a cross-polarized configuration.

Finally, we have developed a numerical split-step scheme for determining the Green functions in a pulsed pump configuration. This opens the parameter space considerably and a careful analysis of a specific system is necessary to design the optimal setup. However, with the preliminary analysis, we have shown that it is possible to considerably optimize the $g_{\text{click}}^{(2)}$ value by taking the relevant physical aspects of an experimental setup into account.

APPENDIX A: NONLINEAR COEFFICIENTS

Here we give a justification for using the vectorial model described by Lin *et al.* [18] to model quantum fields quantized in arbitrary spatial or polarization modes. We start by considering the full-vectorial Hamiltonian describing the electronic interaction, and Raman scattering [25],

$$\hat{H}_{\text{e}} = \int d^3\mathbf{x} \frac{1}{4\varepsilon^3} \sum_{ijkl} \chi_{ijkl}^{(3)} : \hat{D}_i \hat{D}_j \hat{D}_k \hat{D}_l : \qquad \text{(A1a)}$$

$$\hat{H}_{\text{R}} = \int d^3\mathbf{x} \int_0^\infty d\omega \sum_{ij} \mathcal{R}_{ij}(\omega) : \hat{D}_i \hat{D}_j \hat{q}(\omega, \mathbf{x}) :, \quad \text{(A1b)}$$

where $\chi_{ijkl}^{(3)}$ is the third-order susceptibility tensor, ε is the material permittivity, $\mathcal{R}_{ij}$ is the Raman response tensor, $\hat{q}$ is the bosonic phonon operator, $\hat{D}_i$ is the ith vector component of the displacement field, and we have defined $\mathbf{x} = (x, y, z)$. In contrast to previous work dealing with Raman scattering, we choose the phonon operator to be localized in all three spatial coordinates $\mathbf{x}$. This gives rise to a multimode description of Raman scattering, which is necessary to construct a model for intermodal FWM-BS. We perform a mode-field expansion of

the fields to find the Hamiltonian in terms of the creation and annihilation operators [39],

$$\hat{\mathbf{D}}(\mathbf{x}, t) = \sum_m \sqrt{\frac{\hbar \varepsilon \omega_m}{2 v_m}} [\hat{A}_m(z, t) \mathbf{d}^{(m)}(\mathbf{r}) e^{i\beta_{m0}z - i\omega_m t} + \text{H.c.}],$$

$$\text{(A2a)}$$

$$\hat{q}(\omega, \mathbf{x}) \propto \hat{b}(\omega, \mathbf{x}) + \hat{b}^\dagger(\omega, \mathbf{x}), \qquad \text{(A2b)}$$

where ω_m and v_m is the center frequency and group velocity of field m, respectively. The mode profiles are normalized, $\int \mathrm{d}^2 \mathbf{r} |\mathbf{d}^{(m)}(\mathbf{r})|^2 = 1$, and are not necessarily orthogonal. Inserting this into the electronic Hamiltonian and keeping only photon-number-conserving terms, we find the mode-field Hamiltonian for the electronic interactions,

$$\hat{H}_{\mathrm{e}} = \hbar \int \mathrm{d}z \left(2 - \tfrac{3}{2}\delta_{abcd}\right) \Gamma_{abcd} \hat{A}_a^\dagger \hat{A}_b^\dagger \hat{A}_c \hat{A}_d, \qquad \text{(A3)}$$

where we have defined the nonlinear coefficient,

$$\Gamma_{abcd} = \frac{3\hbar}{4\varepsilon} \sqrt{\frac{\omega_a \omega_b \omega_c \omega_d}{v_a v_b v_c v_d}} \sum_{ijkl} \chi_{ijkl}^{(3)} O_{ijkl}^{(abcd)}, \qquad \text{(A4)}$$

$$O_{ijkl}^{(abcd)} = \int \mathrm{d}^2 \mathbf{r} \, d_i^{(a)*}(\mathbf{r}) d_j^{(b)*}(\mathbf{r}) d_k^{(c)}(\mathbf{r}) d_l^{(d)}(\mathbf{r}), \qquad \text{(A5)}$$

where $O_{ijkl}^{(abcd)}$ is the inverse mode area. Similarly, we find the Raman scattering Hamiltonian in terms of the creation and annihilation operators,

$$\hat{H}_{\mathrm{R}} = \hbar \int \mathrm{d}^3 \mathbf{x} \int_0^\infty \mathrm{d}\omega$$
$$\times \sum_{ij} \mathcal{R}_{ij}(\omega) d_i^{(a)*}(\mathbf{r}) d_j^{(b)}(\mathbf{r}) \hat{q}(\mathbf{x}, \omega) \hat{A}_a^\dagger \hat{A}_b + \text{H.c.} \quad \text{(A6)}$$

Following the procedure outlined by Drummond [25] and Lin *et al.* [18], we arrive at the evolution equation of the quantum fields,

$$\partial_z \hat{A}_m = -\beta_{1m} \partial_t \hat{A}_m - \frac{i}{2} \beta_{2m} \partial_t^2 \hat{A}_m$$
$$+ i \sum_{nkl} \Gamma_{mnkl} (2 - \delta_{mn}) \hat{A}_n^\dagger \hat{A}_k \hat{A}_l + i \sum_n \hat{m}_{mn} \hat{A}_n$$
$$+ i \sum_{nkl} \hat{A}_n \int \mathrm{d}t' f_{mnkl}(t - t') \hat{A}_k^\dagger(t') \hat{A}_l^\dagger(t'), \qquad \text{(A7)}$$

where the noise operator, describing spontaneous Raman scattering, is given by

$$\hat{m}_{mn}(z, t) = \int_0^\infty \mathrm{d}\omega \mathcal{R}_{ij}(\omega) \int \mathrm{d}^2 \mathbf{r} \, d_i^{(n)*}(\mathbf{r}) d_j^{(m)}(\mathbf{r})$$
$$\times [\hat{b}(\mathbf{x}, \omega) e^{-i\omega t} + \hat{b}^\dagger(\mathbf{x}, \omega) e^{i\omega t}] e^{i(\omega_m - \omega_n)t}, \quad \text{(A8)}$$

and the Raman response function is found to be

$$f_{abcd}(t) = 2\Theta(t) e^{i(\omega_a - \omega_b)t} \int_0^\infty \mathrm{d}\omega \sin(\omega t) \mathrm{Im}[f_{abcd}(\omega)],$$

$$\text{(A9a)}$$

$$\mathrm{Im}[f_{abcd}(\omega)] = \sum_{ijkl} \mathcal{R}_{ij}(\omega) \mathcal{R}_{kl}(\omega) O_{ijkl}^{(abcd)}. \qquad \text{(A9b)}$$

The response function and the phonon noise oscillate at the frequency difference, $\omega_a - \omega_b$. When the field is chosen to be the four fields described in Fig. 1, this corresponds to the frequency detuning Ω. When introducing the semiclassical approximation, the nonlinear coefficient becomes

$$\gamma_{abcd} = \frac{\Gamma_{abcd}}{\hbar \sqrt{\omega_a \omega_c}}, \qquad \text{(A10)}$$

where a and c are the pump fields. In the Raman response functions, the coefficient $(\hbar \sqrt{\omega_a \omega_c})^{-1}$ is absorbed into the Raman response tensor $\mathcal{R}_{ij}$.

APPENDIX B: COMMUTATION RELATIONS

In a quantum-mechanical model, the commutation relations should be preserved throughout the evolution. However, since the loss is introduced through the delayed response function, this can no longer be the case. Here, we will show that the commutation relations are preserved to first order in the Raman response, which will suffice for our semiclassical model, as it is experimentally preferred to minimize the Raman interaction.

We consider here the commutation relations in the case of cw pumps. Using Eq. (12), we start out by noting

$$[\hat{a}_{\mathrm{i}}(\ell, \omega), \hat{a}_{\mathrm{i}}(\ell, \omega')] = [\hat{a}_{\mathrm{i}}(\ell, \omega), \hat{a}_{\mathrm{s}}(\ell, \omega')] = 0, \qquad \text{(B1)}$$

for all ℓ, since $[\hat{m}_{\mathrm{i}}(z, \omega), \hat{m}_{\mathrm{s}}(z', \omega')] = 0$, which can easily be shown by Fourier transforming Eq. (A8).

Next, we Taylor expand the Green functions, given by Eq. (13), in the Raman response $g_i = \sqrt{2\pi} \mathrm{Im}\{g\}\ell$,

$$G_{\mathrm{ii}} = \cos(g_r) - g_i e^{ig_r} + O(g_i^2), \qquad \text{(B2)}$$

$$G_{\mathrm{is}} = i \sin(g_r) - g_i e^{ig_r} + O(g_i^2), \qquad \text{(B3)}$$

where $g_r = \sqrt{2\pi} \mathrm{Re}\{g\}\ell$. We can thereby determine the commutation relation to first order in the Raman response g_i,

$$[\hat{a}_{\mathrm{i}}(\ell, \omega), \hat{a}_{\mathrm{s}}^\dagger(\ell, \omega')] = g_i [n_{\mathrm{th}}(\omega - \Omega) - 2]\delta(\omega - \omega') + O(g_i^2).$$

$$\text{(B4)}$$

The term with n_{th} originates from $[\hat{m}_{\mathrm{i}}(z, \omega), \hat{m}_{\mathrm{s}}^\dagger(z', \omega')] = \sqrt{2\pi} \mathrm{Im}[g(\omega)] n_{\mathrm{th}}(\omega - \Omega)\delta(\omega - \omega')\delta(z - z')$ and captures the gain induced by spontaneous Raman scattering. The term with -2 describes the loss induced by stimulated Raman scattering. Similarly, it can be found that $[\hat{a}_{\mathrm{i}}(\ell, \omega), \hat{a}_{\mathrm{i}}^\dagger(\ell, \omega')] = \delta(\omega - \omega') + O(g_i)$. Thereby, we have shown that in the perturbative regime, $|g_i| \ll 1$, the commutation relations are preserved.

APPENDIX C: SECOND-ORDER CORRELATION FUNCTION

We want to find an expression for the second-order correlation function in terms of the Green functions. To simplify the evaluation, we express the output idler operator in terms of two operators, representing the optical and phononic parts,

respectively,

$$\hat{a}_{\mathrm{i}}(\ell, t) = \hat{\mathcal{A}}(t) + i\hat{\mathcal{M}}(t). \tag{C1}$$

Using that $\langle\hat{\mathcal{M}}\rangle = 0$, we determine the four-point correlation for a single-photon input state, which thereby yields

$$
\begin{aligned}
\langle\hat{a}_{\mathrm{i}}^{\dagger}&(t_1)\hat{a}_{\mathrm{i}}^{\dagger}(t_2)\hat{a}_{\mathrm{i}}(t_2)\hat{a}_{\mathrm{i}}(t_1)\rangle \\
&= |\psi_{\mathrm{out}}(t_1)|^2 E(t_2, t_2) + |\psi_{\mathrm{out}}(t_2)|^2 E(t_1, t_1) \\
&\quad + \psi_{\mathrm{out}}^*(t_1)\psi_{\mathrm{out}}(t_2)E(t_2, t_1) \\
&\quad + \psi_{\mathrm{out}}^*(t_2)\psi_{\mathrm{out}}(t_1)E(t_1, t_2) \\
&\quad + \langle\hat{\mathcal{M}}^{\dagger}(t_1)\hat{\mathcal{M}}^{\dagger}(t_2)\hat{\mathcal{M}}(t_2)\hat{\mathcal{M}}(t_1)\rangle,
\end{aligned} \tag{C2}
$$

where we have used the optical four-point correlation function and the correlation function odd number of creation or annihilation operators evaluate to zero, and we have defined the expectation values as

$$E(t_1, t_2) = \langle\hat{\mathcal{M}}^{\dagger}(t_1)\hat{\mathcal{M}}(t_2)\rangle, \tag{C3a}$$

$$\psi_{\mathrm{out}}^*(t_1)\psi_{\mathrm{out}}(t_2) = \langle\hat{\mathcal{A}}^{\dagger}(t_1)\hat{\mathcal{A}}(t_2)\rangle. \tag{C3b}$$

The phononic four-point correlation function can be factorized since the phonon's bath exhibits thermal statistics,

$$
\begin{aligned}
\langle\hat{\mathcal{M}}^{\dagger}&(t_1)\hat{\mathcal{M}}^{\dagger}(t_2)\hat{\mathcal{M}}(t_2)\hat{\mathcal{M}}(t_1)\rangle \\
&= E(t_1, t_1)E(t_2, t_2) + E(t_1, t_2)E(t_2, t_1),
\end{aligned} \tag{C4}
$$

and thereby we obtain the numerator of Eq. (7).

[1] E. Knill, R. Laflamme, and G. J. Milburn, A scheme for efficient quantum computation with linear optics, Nature (London) **409**, 46 (2001).

[2] D. P. DiVincenzo and IBM, The physical implementation of quantum computation, Fortschr. Phys. **48**, 771 (2000).

[3] T. D. Ladd, F. Jelezko, R. Laflamme, Y. Nakamura, C. Monroe, and J. L. O'Brien, Quantum computers, Nature (London) **464**, 45 (2010).

[4] J. M. Lukens and P. Lougovski, Frequency-encoded photonic qubits for scalable quantum information processing, Optica **4**, 8 (2017).

[5] L. Ma, O. Slattery, and X. Tang, Single photon frequency up-conversion and its applications, Phys. Rep. **521**, 69 (2012).

[6] T. van Leent, M. Bock, F. Fertig, R. Garthoff, S. Eppelt, Y. Zhou, P. Malik, M. Seubert, T. Bauer, W. Rosenfeld, W. Zhang, C. Becher, and H. Weinfurter, Entangling single atoms over 33 km telecom fibre, Nature (London) **607**, 69 (2022).

[7] N. Maring, P. Farrera, K. Kutluer, M. Mazzera, G. Heinze, and H. de Riedmatten, Photonic quantum state transfer between a cold atomic gas and a crystal, Nature (London) **551**, 485 (2017).

[8] H. J. McGuinness, M. G. Raymer, and C. J. McKinstrie, Theory of quantum frequency translation of light in optical fiber: Application to interference of two photons of different color, Opt. Express **19**, 17876 (2011).

[9] X. Wang, X. Jiao, B. Wang, Y. Liu, X.-P. Xie, M.-Y. Zheng, Q. Zhang, and J.-W. Pan, Quantum frequency conversion and single-photon detection with lithium niobate nanophotonic chips, npj Quantum Inf. **9**, 38 (2023).

[10] M. T. Hansen, E. Z. Ulsig, F. Labbé, M. L. Madsen, Y. Ding, K. Rottwitt, and N. Volet, Efficient and robust second-harmonic generation in thin-film lithium niobate using modal phase matching, Front. Photon. **4**, 1324648 (2023).

[11] K. Inoue, Tunable and selective wavelength conversion using fiber four-wave mixing with two pump lights, IEEE Photon. Technol. Lett. **6**, 1451 (1994).

[12] A. Farsi, S. Clemmen, S. Ramelow, and A. L. Gaeta, Low-noise quantum frequency translation of single photons, in *CLEO: 2015* (Optica Publishing Group, San Jose, CA, 2015), p. FM3A.4.

[13] A. S. Clark, S. Shahnia, M. J. Collins, C. Xiong, and B. J. Eggleton, High-efficiency frequency conversion in the single-photon regime, Opt. Lett. **38**, 947 (2013).

[14] C. Joshi, A. Farsi, S. Clemmen, S. Ramelow, and A. L. Gaeta, Frequency multiplexing for quasi-deterministic heralded single-photon sources, Nat. Commun. **9**, 847 (2018).

[15] C. Joshi, A. Farsi, and A. Gaeta, Hong-Ou-Mandel interference in the frequency domain, in *Conference on Lasers and Electro-Optics* (Optica Publishing Group, San Jose, California, 2017), p. FF2E.3.

[16] S. Clemmen, A. Farsi, S. Ramelow, and A. L. Gaeta, Ramsey interference with single photons, Phys. Rev. Lett. **117**, 223601 (2016).

[17] K. Krupa, A. Tonello, V. V. Kozlov, V. Couderc, P. Di Bin, S. Wabnitz, A. Barthélémy, L. Labonté, and S. Tanzilli, Bragg-Scattering conversion at telecom wavelengths towards the photon counting regime, Opt. Express **20**, 27220 (2012).

[18] Q. Lin, F. Yaman, and G. P. Agrawal, Photon-pair generation in optical fibers through four-wave mixing: Role of Raman scattering and pump polarization, Phys. Rev. A **75**, 023803 (2007).

[19] J. G. Koefoed, J. B. Christensen, and K. Rottwitt, Effects of noninstantaneous nonlinear processes on photon-pair generation by spontaneous four-wave mixing, Phys. Rev. A **95**, 043842 (2017).

[20] S. M. M. Friis, L. Mejling, and K. Rottwitt, Effects of Raman scattering and attenuation in silica fiber-based parametric frequency conversion, Opt. Express **25**, 7324 (2017).

[21] J. Bonetti, A. D. Sánchez, S. M. Hernandez, and D. F. Grosz, A simple approach to the quantum theory of nonlinear fiber optics, arXiv:1902.00561.

[22] R. Hellwarth, Third-order optical susceptibilities of liquids and solids, Prog. Quantum Electron. **5**, 1 (1977).

[23] K. Rottwitt, J. G. Koefoed, K. Ingerslev, and P. Kristensen, Inter-modal Raman amplification of OAM fiber modes, APL Photon. **4**, 030802 (2019).

[24] P. D. Drummond and J. F. Corney, Quantum noise in optical fibers. I. Stochastic equations, J. Opt. Soc. Am. B **18**, 139 (2001).

[25] P. D. Drummond, Quantum theory of fiber-optics and solitons, in *Coherence and Quantum Optics VII*, edited by J. H. Eberly, L. Mandel, and E. Wolf (Springer US, Boston, MA, 1996), pp. 323–332.

[26] A. K. Ekert and P. L. Knight, Relationship between semiclassical and quantum-mechanical input-output theories of optical response, Phys. Rev. A **43**, 3934 (1991).

[27] B. Yurke, Input-Output Theory, in *Quantum Squeezing*, edited by P. D. Drummond and Z. Ficek (Springer, Berlin, 2004), pp. 53–96.

[28] A. Christ, K. Laiho, A. Eckstein, K. N. Cassemiro, and C. Silberhorn, Probing multimode squeezing with correlation functions, New J. Phys. **13**, 033027 (2011).

[29] R. H. Stolen, J. P. Gordon, W. J. Tomlinson, and H. A. Haus, Raman response function of silica-core fibers, J. Opt. Soc. Am. B **6**, 1159 (1989).

[30] R. Schiek, Nonlinear refractive index in silica glass, Opt. Mater. Express **13**, 1727 (2023).

[31] I. Esmaeil Zadeh, J. W. N. Los, R. B. M. Gourgues, J. Chang, A. W. Elshaari, J. R. Zichi, Y. J. van Staaden, J. P. E. Swens, N. Kalhor, A. Guardiani, Y. Meng, K. Zou, S. Dobrovolskiy, A. W. Fognini, D. R. Schaart, D. Dalacu, P. J. Poole, M. E. Reimer, X. Hu, S. F. Pereira *et al.*, Efficient single-photon detection with 7.7 ps time resolution for photon-correlation measurements, ACS Photon. **7**, 1780 (2020).

[32] P. Lodahl, S. Mahmoodian, and S. Stobbe, Interfacing single photons and single quantum dots with photonic nanostructures, Rev. Mod. Phys. **87**, 347 (2015).

[33] D. V. Reddy, M. G. Raymer, and C. J. McKinstrie, Sorting photon wave packets using temporal-mode interferometry based on multiple-stage quantum frequency conversion, Phys. Rev. A **91**, 012323 (2015).

[34] L. Mejling, D. S. Cargill, C. J. McKinstrie, K. Rottwitt, and R. O. Moore, Effects of nonlinear phase modulation on Bragg scattering in the low-conversion regime, Opt. Express **20**, 27454 (2012).

[35] Wave propagation in optical fibers, in *Nonlinear Fiber Optics*, edited by G. Agrawal (Academic Press, Amsterdam, 1995), pp. 28–59.

[36] C. J. McKinstrie, L. Mejling, M. G. Raymer, and K. Rottwitt, Quantum-state-preserving optical frequency conversion and pulse reshaping by four-wave mixing, Phys. Rev. A **85**, 053829 (2012).

[37] L. Mejling, C. J. McKinstrie, M. G. Raymer, and K. Rottwitt, Quantum frequency translation by four-wave mixing in a fiber: Low-conversion regime, Opt. Express **20**, 8367 (2012).

[38] M. Guasoni, F. Parmigiani, P. Horak, J. Fatome, and D. J. Richardson, Intermodal four-wave mixing and parametric amplification in kilometer-long multimode fibers, J. Lightwave Technol. **35**, 5296 (2017).

[39] N. Quesada, L. G. Helt, M. Menotti, M. Liscidini, and J. E. Sipe, Beyond photon pairs: Nonlinear quantum photonics in the high-gain regime, Adv. Opt. Photon. **14**, 291 (2022).